THE JOURNAL OF PHYSICAL CHEMISTRY A
A JOURNAL OF THE AMERICAN CHEMICAL SOCIETY

pubs.acs.org/JPCA

Article

Charge Effects on the Photodegradation of Single Optically Trapped Oleic Acid Aerosol Droplets

Published as part of The Journal of Physical Chemistry virtual special issue "Advances in Atmospheric Chemical and Physical Processes".

Evelyne A. Parmentier, Pablo Corral Arroyo, Richard Gruseck, Loren Ban, Grégory David, and Ruth Signorell*

Cite This: *J. Phys. Chem. A* 2022, 126, 4456–4464

Read Online

ACCESS | Metrics & More | Article Recommendations | Supporting Information

ABSTRACT: It has recently been reported that reactions can occur faster in microdroplets than in extended condensed matter. The electric charge of droplets has also been suggested as a possible cause of this phenomenon. Here, we investigate the influence of electric charges on the photodegradation of single, optically trapped oleic acid aerosol droplets in the absence of other reactive species. The temporal evolution of the chemical composition and the size of droplets with charge states ranging from 0 to 10^4 elementary charges were retrieved from Raman spectra and elastic light scattering, respectively. No influence of the droplet charge was observed, either on the chemical composition or on the kinetics. Based on a kinetic multilayer model, we propose a reaction mechanism with the photoexcitation of oleic acid into an excited state, subsequent decay into intermediates and further photoexcitation of intermediates and their decay into nonvolatile and volatile products.

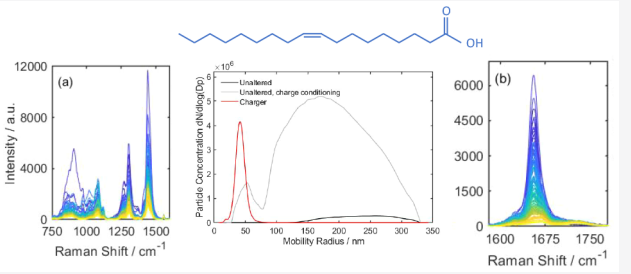

1. INTRODUCTION

The composition of atmospheric aerosol particles is very complex, and it is constantly altered as they interact with gas phase components and sunlight. Organic aerosol particles constitute a significant fraction of atmospheric aerosols.[1,2] With their diverse functional groups absorbing light in the ultraviolet/visible range, organic aerosols are prone to photochemical processes.[3−9] Because of the diversity of the chemical composition of organic aerosols, laboratory investigations often use model systems to characterize the behavior of certain classes of organic aerosols. Oleic acid (OA), for example, has often been used as a proxy to investigate the (photo)chemistry of unsaturated fatty acid in the form of aerosol particles. Notably, the reactions of aerosol particles comprised of OA with ozone or other reactive gases, including nitrogen oxides and hydroxyl radicals, have been studied in detail.[10−16]

We have recently reported on the photochemistry of OA droplets in the absence of highly reactive gaseous species.[17,18] These studies were performed on single OA droplets immobilized in optical traps. We found that photodegradation of OA was induced by the trapping lasers at visible wavelengths of 532 and 660 nm. Time-dependent Raman spectra recorded during the photodegradation revealed characteristic changes in the region of the C=C double bond (~1655 cm^{-1}), which occurred faster at higher trapping laser power and shorter wavelength.[17] The photodegradation was accompanied by a pronounced decrease of the droplet size with time, hinting at the formation of volatile products that evaporate from the droplets. Furthermore, the kinetics did not show any significant dependence on the oxygen amount in the gas phase or on the size of the droplets. On the basis of these observations, we suggested a reaction mechanism with photoexcited OA* as the reactive species in the dominant pathway, which then proceeded via unimolecular decay into intermediates I or through reaction with ground state OA. The further reaction steps to the products P could not be specified.[17]

Another interesting observation was the pronounced scatter observed for the reaction kinetics of individual droplets at apparently similar conditions.[17] The droplet size could be excluded as origin for the observed scatter, as we did not find a correlation between reaction kinetics and droplet size. Electric charging of the droplets was put forward as another explanation for the pronounced scatter of the reaction kinetics of individual droplets. During the droplet formation by atomization, a fraction of the droplets are electrically charged.[19−21] It has recently been

Received: February 25, 2022
Revised: June 15, 2022
Published: June 29, 2022

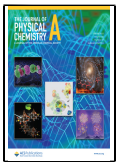

https://doi.org/10.1021/acs.jpca.2c01370
J. Phys. Chem. A 2022, 126, 4456−4464

suggested that certain reactions are accelerated when they take place in sprayed or levitated microdroplets compared with corresponding reactions in the extended condensed phase.[22−29] We have demonstrated and quantified the acceleration of photochemical reactions in single aerosol particles caused by light enhancement inside the particles due to optical resonance phenomena.[30,31] However, in other cases where acceleration of a reaction was observed in droplets, its origin remained unclear and open to discussions.[23,28,32,33] One factor that was discussed is the electric charge state of the droplets formed by electrospraying.[29,34−37] Several mechanisms were suggested to explain these charge effects on the reaction rates: The electric field inside the droplet directly affects the transition state, and the energy profile of chemical reaction can be changed leading to catalysis of reactions. A strong field inside the droplet may support the removal of bonded electrons, facilitating redox processes in aqueous microdroplets. The electric field changes the alignment of molecules near the interface, thereby reducing the entropic barrier of chemical reactions in microdroplets.

The aim of the present study is 2-fold: (i) We investigate the influence of electric charge on the photodegradation of OA droplets by actively charging and discharging the droplet ensemble to clarify whether the electric charge could be the cause of the scatter of the reaction rates observed between individual droplets. (ii) We refine the reaction mechanism of the OA photodegradation proposed in ref 17 by fitting a kinetic multilayer model to the time-dependent concentrations of reactant (OA), intermediates I and products P retrieved from the experimental Raman spectra and to the time-dependent decrease of the droplet size observed by elastic scattering.

2. EXPERIMENTAL METHODS

2.1. Optical Trapping and Droplet Characterization Methods. A detailed description of the experimental methods used in the present work can be found in our previous publication on the photochemistry of single optically trapped oleic acid (OA) droplets.[17] As in our previous work, single pure OA droplets were trapped in the trapping cell by counter-propagating optical tweezers (Figure 1) using a 532 nm trapping laser. The experiments were conducted in a controlled dry synthetic air (N_2/O_2 = 4/1) gas environment by maintaining a constant gas flow through the trapping cell. The photo-degradation of the OA droplets was induced by the trapping laser, in the absence of any highly reactive species such as ozone. Figure S5 in the Supporting Information shows the UV−vis absorption spectrum of oleic acid. The absorption of 532 nm light by the oleic acid is weak but nonzero, and it is sufficient to explain the observed photochemistry. This spectrum has also been used to estimate the imaginary part of its refractive index (k), which is approximately 10^{-8}.

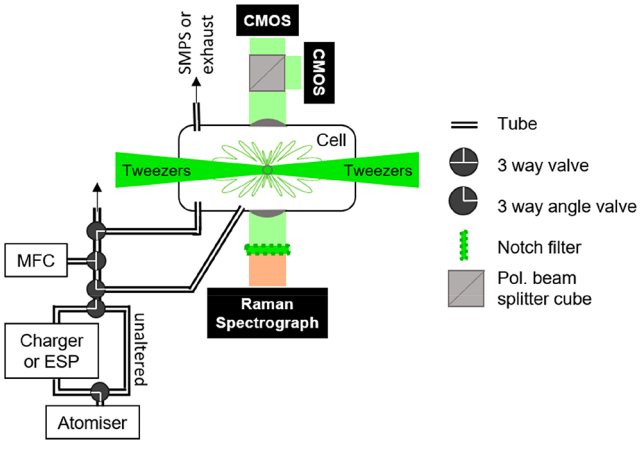

Figure 1. Trapping cell and the charging devices. ESP = electrostatic precipitator. MFC = mass flow controller. [adapted from Figure 1b in ref 17 under Creative Commons CC-BY licensing agreement]

Raman scattering of the trapping laser by the droplet was used to monitor the time-dependent chemical composition of the droplets during the photodegradation. For that purpose, the inelastically scattered light was collected by a spectrograph (Figure 1). Cosmic ray removal and background correction was applied to each Raman spectrum before data analysis. The temporal evolution of the droplet size was retrieved from the trapping laser light that was elastically scattered by the particle over an angular range of the scattering angle of 90 ± 24.8°. The elastically scattered light was split by a polarization beam splitter cube (Figure 1) to record polarization resolved two-dimensional angular optical scattering (TAOS) images. Polarization- and time-resolved TotalTAOS signals were obtained by integration over the TAOS images (see examples in Figure 2 in ref 17). The time-dependent decrease of the droplet radius, R, was determined from a fit using Mie theory, assuming a constant refractive index of m = 1.48[17,18] and a third order polynomial for the temporal change of the droplet radius, $R(t) = A + Bt + Ct^2 + Dt^3$.

2.2. Droplet Generation and Electric Charging. OA aerosol droplets with radii $R_{initial}$ in the range between 20 to 300 nm were generated in an atomizer (model 3076 by TSI).[38] Then, the droplets entered the trapping cell either without modification of their original charge state ("unaltered"), or after active charging by a unipolar aerosol charger ("charged"), or as uncharged droplets after passing an electrostatic precipitator ("neutral") (Figure 1). Atomization of liquids can result in aerosols ("unaltered") that, in addition to a high fraction of uncharged droplets, contain a non-negligible portion of charged droplets with unknown charge distribution.[20,21] To reach high electric charge states of controlled polarity (charged droplets), active charging of the droplet is required. Charged droplets of positive polarity were generated in a home-built positive corona-wire unipolar aerosol charger.[20,39,40] As described in the next paragraph, we determined the approximate charge and size distribution of the unaltered droplets and the charged droplets with a Scanning Mobility Particle Sizer (SMPS, model 3938 by TSI) (see Supporting Information for further information about the SMPS and related quantities such as electrical mobility and mobility radius). The "neutral" droplets were obtained by removing charged droplets from the aerosol flow in a home-built electrostatic precipitator.[20,39,41] By applying the voltage up to 4 kV, charged droplets of both polarities were lost by deposition on the precipitator walls.

Most droplets that reached the trapping cell were not trapped, but left the cell again through the exhaust, where they were analyzed with the SMPS (Figure 1). Results of this analysis are shown in Figure 2. The droplet size distribution after atomization is the same for all three cases (neutral, unaltered, charged). To determine the droplet size distribution (see also Ban *et al.*[42]), we analyzed the unaltered aerosol after the exhaust with the SMPS using a charge conditioner (X-ray neutralizer) and the multiple charge correction as implemented in the SMPS software. The use of the X-ray neutralizer and the charge corrections is referred to as "charge conditioning". This size

https://doi.org/10.1021/acs.jpca.2c01370
J. Phys. Chem. A 2022, 126, 4456−4464

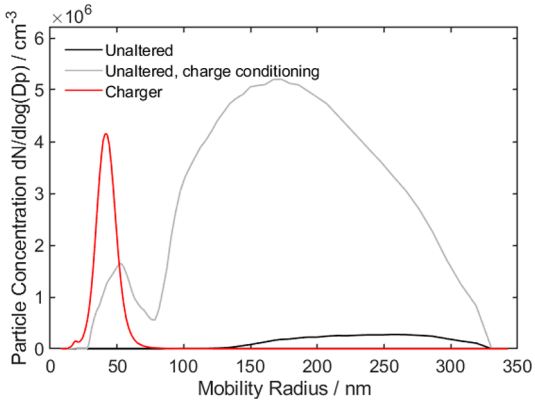

Figure 2. Mobility radius of atomized aerosol droplets which are "unaltered" after the atomizing process (black and gray line) and droplets which are "charged" after the atomizing droplets (red line).

distribution is shown as gray line in Figure 2. It spans droplet radii $R_{initial}$ from ∼25 to ∼300 nm, with a maximum at ∼175 nm.

Information on the fraction of positively charged droplets in the unaltered aerosol was obtained by SMPS measurements without charge conditioning (black line in Figure 2). Neutral droplets cannot be detected by the SMPS under these conditions. The same holds for negatively charged droplets since the SMPS was operated with negative polarity. Therefore, the comparison of the gray and black lines in Figure 2 reveals that only a very small portion of the droplets acquires only low positive charges in the atomization process (see Supporting Information). The small portion of positively charged droplets is obvious from the much lower particle concentration of the black compared with the gray line. The fact that the major peak in the black distribution is not pronouncedly shifted toward smaller mobility radii (higher electrical mobility) compared with the gray distribution indicates that the average charge state of the aerosol droplets is much lower than 1 ($=q_{initial,unaltered}$). Even though we cannot measure the fraction of negatively charged particles, their portion is very likely similarly small[43] as the one of the positively charged droplets. Consequently, the unaltered aerosol mainly consists of uncharged droplets with only a small fraction of charged droplets.

This behavior changes for the charged aerosol, for which many droplets carry a substantial amount of positive charge (red line in Figure 2). The charged aerosol was measured with the SMPS operated with negative polarity, and without charge conditioning, i.e., in an operation mode in which only positively charged droplets are detected. The large shift of the original size distribution (gray line) to smaller mobility radius (higher electrical mobilities) centered at ∼40 nm in radius upon charging (red line) indicates that the droplets acquired a significant amount of positive charges in the charger. Here we make a simple estimation of the particle charge state in the charged aerosol sample. This is performed by selecting three droplet radii $R_{initial}$ that represent the size distribution: 150 nm for its mean, and 50 and 300 nm for its lower and upper limits, respectively. By using electrical mobility theory (i.e., eq S1 in the Supporting Information), we then calculate the average charge state that would result in an electrical mobility centered at 40 nm (red line in Figure 2). Droplet radii $R_{initial}$ of 50, 150, and 300 nm correspond to the average charge state $q_{initial,charged}$ of 2 ± 1, 10 ± 6, and 24 ± 15, respectively (uncertainties are estimated from the one standard deviation of the mobility distribution corresponding to the charged distribution, red line in Figure 2). The acquired particle charges change approximately linearly with the particle radius, as observed in ref 40 using a similar charger. Evidently, the fraction of charged droplets is substantially higher in charged aerosol compared with the unaltered aerosol, and the droplets carry much higher charges.

Important for the present study is the fact that the size (R) and thus the charge state of the trapped droplets substantially exceeds that of the droplets that enter and exit the trapping cell, i.e., the droplets that were characterized in the previous paragraphs ($R_{initial}$). This was caused by the optical force, which pushed smaller droplets toward the trapping position, where they coagulated to form a single large droplet. The occurrence of particle coagulation was confirmed by observations of stepwise increases in the number of fringes in recorded TAOS patterns. The initial radius R of these single trapped droplets was determined from TotalTAOS measurements to lie in the region from ∼1200 to 1850 nm. Taking into account the particle size and charge distributions and assuming that all particle sizes are equally probable to coagulate, a Monte Carlo simulation (see Supporting Information) was performed to determine the size and charge state of the large trapped droplet after coagulation. For the unaltered and charged aerosol between 300 and 1300 small droplets ($R_{initial}$ is in the range from 50 to 300 nm) coagulate to form a large droplet. The charge state of the trapped unaltered droplets is a Gaussian distribution with mean 0 and a widths of less than a few tens of elementary charges. For the charged aerosol, by contrast, the charge state of the large trapped droplets is in the range between 3000 and 13000 elementary charges. Using formulas presented in ref 44, we estimated the repulsive Coulomb force hindering the coagulation of droplets with charge of the same sign and compared it with the optical scattering force which induces their coagulation. The scattering force is calculated using the formula presented in ref 45. For the droplet radii and charge states considered in this paper (one droplet between 25 and 350 nm in radius with charges between 2 and 30 charges and one droplet between 20 and 1850 nm in radius with charges up to 13500 for the larger particles), the scattering force exceeds the repulsion force by approximately 1 order of magnitude or more. Hence, the coagulation of droplets with charge of the same sign is not significantly hindered in our experiments.

2.3. Kinetic Multilayer Model. In order to obtain a better qualitative understanding of the observed photochemical reaction in the OA droplets, a kinetic multilayer model was implemented.[46] It provides a depth-resolved description of chemical reactions and mass transport in trapped microparticles. The model resolves the chemical reactions, diffusion of key compounds through the particle, diffusion to the sorption layer, the evaporation of volatile compounds from the sorption layer, and the evolution of the particle size.

The model divides the particle in four equally thick layers and a sorption layer of 1 nm that describes the droplet surface.[46] Bulk diffusion is treated explicitly as fluxes ($F_{i,i\pm1}$) from one layer (i) to the next ($i \pm 1$). The sorption layer can only exchange volatile compounds with the particle and the surroundings. Transport velocities (k_{diff}) can be derived from the corresponding bulk diffusion coefficients (D) by considering the average distance traveled by diffusing molecules in one direction and the average time required to travel over this distance by diffusion.[46,47] The mass fluxes between layers are then given by

$$F_{i,i\pm1} = k_{diff}[C]_{i,t} = \frac{4D}{\pi d}[C]_{i,t} \quad (1)$$

https://doi.org/10.1021/acs.jpca.2c01370
J. Phys. Chem. A 2022, 126, 4456−4464

where d is the layer thickness and $[C]_{i,t}$ is the concentration of a species C in layer i at time t.

The model calculates the change in the concentration of each compound in each layer as a function of time by retrieving the fluxes from and into the two adjacent layers for small time steps ($\Delta t = 10^{-6}$ s) using Fick's diffusion equation. Fickian diffusion is a continuum approach which only applies for random molecular motion. By choosing a sufficiently high number of layers, continuum conditions can be achieved. $[C]_{i,t+\Delta t}$ is calculated considering both the diffusion-related change in the concentration and the change in concentration due to the reaction:

$$[C]_{i,t+\Delta t} = [C]_{i,t} + \left(P_{C,i} - L_{C,i} + F_{i-1,i}\frac{A_i}{V_i} + F_{i+1,i}\frac{A_{i+1}}{V_i} - F_{i,i-1}\frac{A_i}{V_i} - F_{i,i+1}\frac{A_{i+1}}{V_i}\right)\Delta t = [C]_{i,t} + P_{C,i}\Delta t - L_{C,i}\Delta t + k_{\text{diff}}\left(([C]_{i-1,t} - [C]_{i,t})\frac{A_i}{V_i} + ([C]_{i+1,t} - [C]_{i,t})\frac{A_{i+1}}{V_i}\right)\Delta t \quad (2)$$

where $P_{C,i}$ and $L_{C,i}$ are the production and loss rates of the species C in the layer i, A_i is the interface area between the layers i and $(i - 1)$, V_i is the volume of the layer i. $P_{C,i}$ and $L_{C,i}$ are from the proposed reaction scheme (see Table 1) that is explained in the subsequent section. The desorption of volatile compounds from the sorption layer, s, is described as a first order decay with a rate proportional to the product of the desorption constant k_{des} and the concentration of C in the sorption layer ($[C]_{s,t}$):

$$[C]_{s,t+\Delta t} = [C]_{s,t} - k_{\text{des}}[C]_{s,t}\Delta t \quad (3)$$

Table 1. Chemical Reactions and the Corresponding Rate Coefficients Used for the Model[s]

parameter/reaction	constant	value/s^{-1}
$OA \xrightarrow{h\nu} OA^*$ (R1)	k_1	0.0002
$OA^* \rightarrow OA$ (R2)	k_2	10^5
$OA^* \rightarrow I$ (R3)	$\boldsymbol{k_3}$	$\mathbf{10^5}$
$I \xrightarrow{h\nu} I^*$ (R4)	k_4	0.0002
$I^* \rightarrow I$ (R5)	$\boldsymbol{k_5}$	$\mathbf{10^5}$
$I^* \rightarrow P + V$ (R6)	k_6	10^5
$P \xrightarrow{h\nu} P^*$ (R7)	k_7	0.0008
$P^* \rightarrow P$ (R8)	$\boldsymbol{k_8}$	$\mathbf{10^5}$
$P^* + OA \rightarrow OA^* + P$ (R9)	k_9	10^5
$P^* + I \rightarrow I^* + P$ (R10)	k_{10}	2.5×10^4
$OA^* \rightarrow 2V$ (R11)	k_{11}	10^5 (model 2 only)

[s]Rate coefficients that were kept constant during the fit are indicated in bold. All other rate constants were fitted. The abbreviations are as followed: oleic acid = OA, intermediate = I, product = P volatile = V, and excited species = *.

3. RESULTS AND DISCUSSION

3.1. Electric Charge Effects. Our previous study investigated the photodegradation of OA droplets by visible light for unaltered aerosols,[17] i.e., for aerosol droplets with radii in the range R = 1200−1850 nm and electric charges of less than a few tens of elementary charges (section 2.2). In our previous study, a pronounced scatter was found for the values of the decay rate of OA molecules for different individual droplets, the origin of which remained unexplained. We could show that the scatter between individual droplets was not caused by the difference in the droplet size (e.g., caused by optical confinement effects). Another explanation might be the variation in the droplet's charge state of the unaltered aerosol. As determined above, the charge state of the unaltered droplets varies between 0 and a few tens of charges. To clarify the potential influence of the charge state, we compare here results for unaltered, neutral and charged aerosols. As in our previous study, we recorded time-dependent Raman spectra and TotalTAOS signals for droplets trapped from the three differently charged aerosols.

Parts a−c of Figure 3 show as an example the temporal evolution of parts of the Raman spectrum for a droplet trapped from the charged aerosol (see Figures S2 and S3 for unaltered and neutral aerosol). These droplets have charge states in the range 10^3−10^4 elementary charges (section 2.2); i.e., they have a much higher charge than droplets from the unaltered aerosol. The Raman signals in parts a−c of Figures 3 decrease over time because molecules continually evaporate from the droplet over time, resulting in a decrease of the droplet radius R (Figure 3f). The same behavior was also observed for droplets from the unaltered and the neutral aerosols, as shown by Figures 5, S2, and S3. The time-dependence of R in Figure 3f was determined from the TotalTAOS signal (section 2.1). The temporal change of the Raman spectrum in the region of the double bond of OA (Figure 3, parts b and d) clearly shows that in addition to droplet shrinking, OA molecules are photodegraded over time by breaking the double bond. First, the main band at 1655 cm^{-1} of the C═C double bond decreases faster than any other Raman band and a shoulder at 1668 cm^{-1} develops over time. Then, both the main band and the shoulder disappear and a broad feature consisting of two broad bands dominates the Raman spectrum in the region of the double bond. Identical trends were observed for droplets of the unaltered and the neutral aerosol, meaning that the same intermediates and products are formed upon photodegradation of the droplets independently of their electric charge state.

To quantify the temporal changes in the region of the double bond, we decomposed the spectra in three time-dependent components as in ref 17: a component that describes intact OA molecules with the double bond at 1655 cm^{-1} (the peak of pure liquid oleic acid), a component that describes intermediate compounds I that produce the shoulder at 1668 cm^{-1} (the shoulder that we observed building up when the experiment was performed in a nitrogen atmosphere with only a few parts per thousand of oxygen), and a component that describes an ensemble of final products P which produce the broad feature with two broad bands that we usually observed in each cases at the end of the photochemical reaction. The same procedure using the same three OA, I, and P components is used for all measurements in this article (neutral, unaltered, and charged droplets). For visualization of this linear decomposition procedure, we display the three components in Figure 3d as blue, red, and yellow lines, respectively, for the Raman spectrum recorded at 10960 s. Figure 3e shows the temporal evolution of the decomposition coefficients of the three components. Note that the quasi-periodic fluctuations on top of relative smooth time-evolution of the linear coefficients arise from whispering gallery modes. These fluctuations are not important for the kinetics because only the smooth time-evolution was considered

https://doi.org/10.1021/acs.jpca.2c01370
J. Phys. Chem. A 2022, 126, 4456−4464

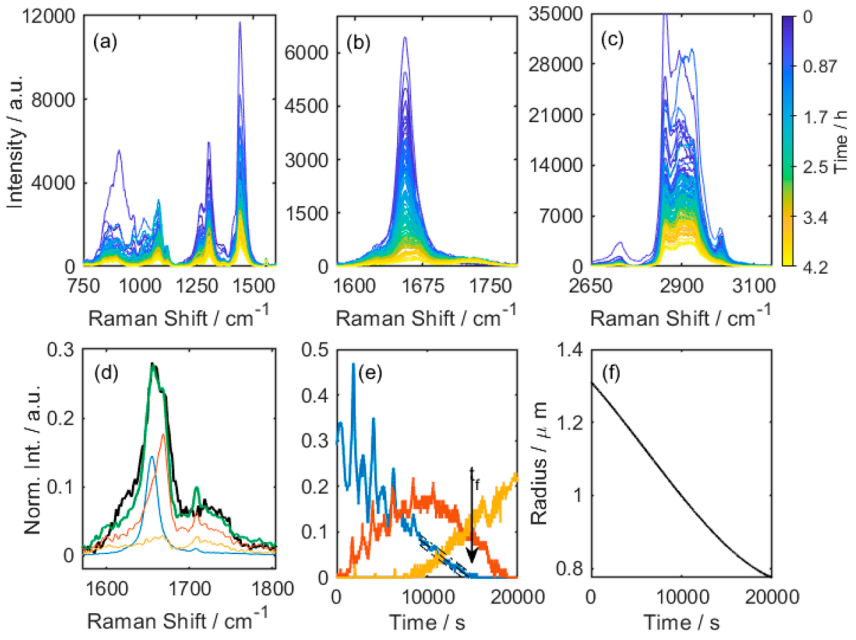

Figure 3. Experimental data and analysis for an example of an optically trapped oleic acid droplet trapped from a charged aerosol. Time-dependent Raman spectrum in the range from (a) 800 to 1500 cm^{-1}, (b) 1600 to 1780 cm^{-1} of the C═C double bond, and (c) 2800 to 3000 cm^{-1}. (d) Linear decomposition of the experimental spectrum (black) into the three components components oleic acid (OA, blue), intermediate (I, red line) and product (P, yellow line). The sum of the three components yields the green spectrum. (e) Temporal evolution of the coefficients of the linear decomposition: OA (blue), I (red line), and P (yellow line). (f) Temporal evolution of the droplet radius R retrieved by elastic light scattering.

(see ref 17 for details). Component OA decreases with time until it disappears completely, component I first increases and then decreases with time until it disappears, while component P is formed into detectable amounts only after the reaction proceeded for some time. P is the only component remaining in the spectrum when OA and I are not present in the spectrum anymore.

Even though the linear decomposition reveals that the same intermediates and products are formed independently of the electric charge state (see above and Figures S2 and S3), this does not mean that the decay times must also be independent of the charge state. By following the same procedure as described in our previous study,[17] we can gain more insight into the reaction kinetics and its dependence on the charge state from an analysis of the time-dependence of component OA. OA decreases linearly toward the end of the reaction (Figure 3e). By fitting this linear tail to a straight line, we obtain a characteristic time t_f at which the decomposition of the OA double bond is completed (within the detection limit) by determining the crossing point of the straight line with the abscissa. Since t_f depends on the laser power and since the latter can vary for different experiments, we use in the following instead of t_f a characteristic time t_f* that has been normalized by the laser power (see, for details, ref 17 and the Supporting Information). The inverse of the normalized characteristic time, $1/t_f$*, is then an indicator of the average reaction rate for the photodegradation of OA.

Figure 4 shows $1/t_f$* for individual droplets trapped from neutral, unaltered and charged aerosols from left to right, respectively. If the charge state were the reason for the observed scatter of the individual data points for the unaltered aerosol in ref 17, we would expect in Figure 4 (i) that the mean values of the reaction rates of the differently charged droplets would pronouncedly vary and (ii) that the scatter for droplets from neutral aerosols would be much less compared with the one observed for unaltered and charged aerosols. From the data in

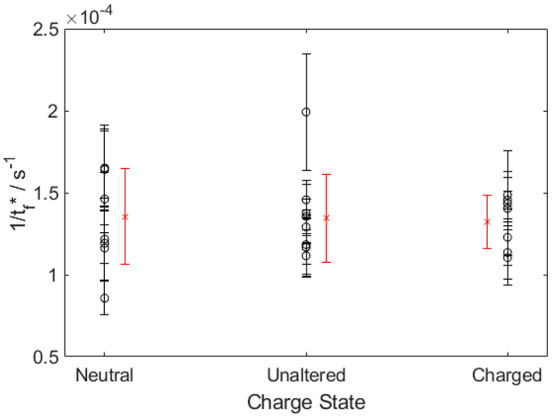

Figure 4. Inverse of the normalized reaction time $1/t_f$* for particles of different charge state. Neutral droplets have no charge, unaltered droplets have charges of less than a few elementary charges, and charged droplets have elementary charges in the range 3000−13000. Circles indicate measurements on individual droplets, and red crosses represent the average values with error bars indicating the standard deviation.

Figure 4, we determine mean values of $1/t_f$* of $(1.41 \pm 0.28) \times 10^{-4}$ s^{-1}, $(1.38 \pm 0.17) \times 10^{-4}$ s^{-1} and $(1.41 \pm 0.3) \times 10^{-4}$ s^{-1} for the neutral, the unaltered, and the charged aerosols, respectively. These mean reaction rates are identical within uncertainties, i. e. there is no detectable influence of the electric charge state on the mean rate. Furthermore, the scatter between individual data points for the neutral, the unaltered and the charged aerosols is also very similar. In particular, there is no reduction of the scatter visible for the neutral aerosol. In fact, the standard deviation (red bars in Figure 4) is largest for the neutral aerosol.

As neither the mean reaction rate nor the scatter of individual data points depend on the charge state, we conclude that the

https://doi.org/10.1021/acs.jpca.2c01370
J. Phys. Chem. A 2022, 126, 4456−4464

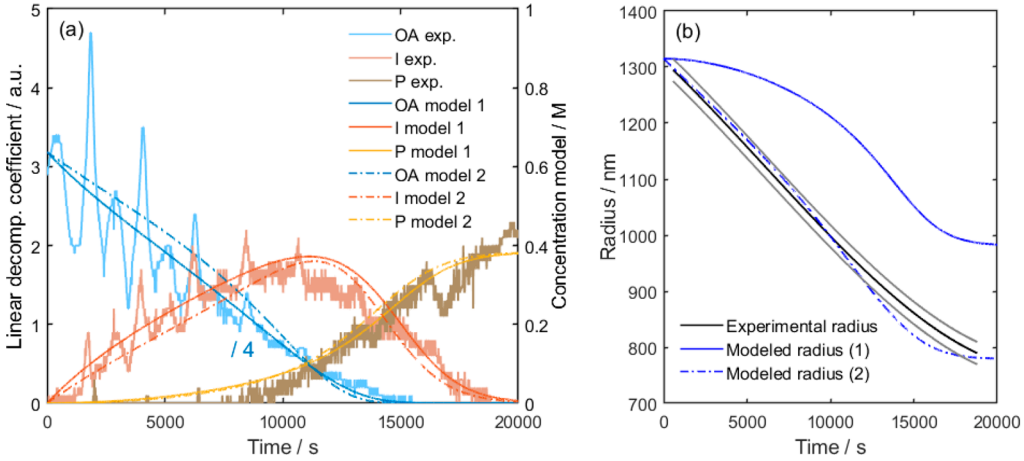

Figure 5. (a) Experimental and simulated temporal evolution of the linear decomposition coefficients of OA, I, and P (see also Figures 3, parts d and e). Two different models, model 1 and model 2 (see Table 1), were employed. (b) Experimental and simulated temporal evolution of the droplet radius.

electric charge is not the reason for the scatter of individual data points and that the charge does not influence the observed photodegradation of OA droplets.

3.2. Reaction Mechanism. In ref 17, we reported the dependence of the photodegradation of OA droplets on the laser power, the laser wavelengths in the visible range (532 and 660 nm), the O_2 content in the surrounding gas phase and the droplet radius. While pronounced increases of the reaction rate were found with increasing laser power and for shorter wavelength, clear dependences on the O_2 content and the droplet radius were not observed. Based on these observations, we suggested a qualitative reaction mechanism (Figure 8 in ref 17 and Figure S5) which involves photoexcited OA* as the reactive species in the dominant pathways. OA* produced by single photon excitation was assumed to decay either directly (unimolecular step) or through reaction with ground state OA into intermediates I. Suggestions for the further reaction steps leading to the final products P were based on the characteristic band of I at 1668 cm^{-1}, which did not show any time-dependence. Since the position of this band coincides with the region where double bonds occur and because of the similarity of the spectrum of I with that of OA in this spectral region, we proposed that I remains a noncyclic aliphatic chain with a double bond. Unimolecular decay of I* to P after photoexcitation of I to I* was proposed as one possible pathway leading from I to P.

Based on these considerations, we have searched for simple, plausible reaction mechanisms that can qualitatively reproduce the temporal evolution of the linear decomposition coefficients of OA, I and P (Figure 3e), and of the droplet radius (Figure 3f). For that purpose, we have fitted different reaction schemes to the experimental data in Figure 3, parts e and f, using the multilayer model (section 2.3). Table 1 contains the elementary reactions and the rate coefficients for the two simplest models (referred to as model 1 and model 2) which reproduce the temporal evolution of the linear decomposition coefficients of OA, I, and P similarly well (see Figure 5a). The only difference between model 1 and 2 is the additional reaction R11 in model 2. This cleavage reaction of photoexcited OA* produces two volatile molecules, V, to enhance droplet evaporation. As Figure 5b shows, the inclusion of this additional reaction is necessary for properly reproducing the temporal reduction of the droplet radius by more than 35%. Apart from that, all other reactions (R1−R10) are identical in models 1 and 2, and are briefly discussed in the following.

Reactions R1 and R2 describe the photoexcitation of OA to OA* and the de-excitation to OA, respectively. Reaction R3 represents a direct (unimolecular) decay of OA* to I. Since the molecules I are assumed to be similar to OA (noncyclic aliphatic chains with a double bond, see above), photoexcitation of I into I* (R4) and de-excitation of I* to I (R5) seem plausible reaction steps. Based on the similarity of the Raman spectra of I and OA, we speculate here that I could have the same length of the aliphatic chain (C18) as OA. The formation of products P is described by reaction R6, which in addition to the formation of nonvolatiles products P (detected in the Raman spectrum) includes the formation of volatile products V. The inclusion of the latter is required to describe droplet evaporation over time. We further speculate that V and P could be degradation products that have suffered a bond breaking next to the double bond (C9). Compared with an exponential decay, the decay of OA and I is accelerated toward the end of the reaction (Figure 5a). Hence, the measurements show that something is accelerating the reaction of OA and I as the reaction proceeds. As both OA and I reactions are accelerated, this could indicate that the products P are involved in further reactions steps, e.g., after photoexcitation to P* (R7) as described by the energy-transfer reactions with OA or I in reactions R9 and R10, respectively. Reactions R7−R10 are necessary to reproduce the observed reaction kinetics of OA and I. The presumed photoexcitation of P might be facilitated by an increase of absorption coefficients due to browning processes, which are often observed for atmospheric aerosol particles.[48,49] For example, the oxidation of gas-phase limonene by ozone produces a variety of compounds with photochemical properties.[50] Carboxylic acids, carbonyl groups, or conjugated systems are the typical functionalities found in the absorbing fraction of the organic compounds in atmospheric aerosol particles.[8]

All rate constants in Table 1 were manually varied during the fitting procedure to reach qualitative agreement with the experimental data, with the exception of the de-excitation constant of OA*, I*, and P* in reactions R2, R5, and R8, respectively. These de-excitation constants were assumed to be 10^5 s^{-1}.[51,52] Furthermore, the values for the molar volumes of OA, I, P, and V ($V_{m,OA}$, $V_{m,I}$, $V_{m,P}$, $V_{m,V}$), the diffusion coefficients of OA, I, and V (D_{OA}, D_I, D_V), and the desorption constant of V (k_{des}) had to be determined. $V_{m,OA}$ was calculated from the density of OA ($V_{m,OA}$ = 0.3139 L/mol). $V_{m,I}$ was assumed to be equal to $V_{m,OA}$ because of the similar nature of these two

https://doi.org/10.1021/acs.jpca.2c01370
J. Phys. Chem. A 2022, 126, 4456−4464

molecular species. $V_{m,P}$ and $V_{m,V}$ were assumed to be the same as the molar volume of azelaic acid (0.1304 L/mol), which is a typical C_9 degradation product of oleic acid. Since the lifetimes of the excited states OA*, I*, and P* are very short (see values above) diffusion was neglected for these species (F in eq 2). The same assumption was made for P because the product formation is homogeneous throughout the droplet. Hence, diffusion was only considered for OA, I, and V. We assumed D_{OA} and D_I to be equal to the diffusion coefficient of oleic acid used in Shiraiwa et al.[46] (10^{-10} cm^2 s^{-1}). $D_V = 3 \times 10^{-7}$ cm^2 s^{-1} was calculated from the Stokes−Einstein relation, assuming a molecule radius of V of 3 Å. For k_{des}, we used the desorption rate for ozone in oleic acid from Shiraiwa et al. (100 s^{-1}). After every second of the simulation, the particle radius was calculated based on the molar volume and concentration of OA, I, P, and V (assuming negligible excited state concentrations), and the layer thickness was recalculated, except for the sorption layer thickness which was held constant at 1 nm.

This model represents a plausible mechanistic scheme that qualitatively reproduces the general trends of the observed photokinetics with minimal complexity: roughly describing the time evolution of the three compounds in the particle (OA, I, and P) and the particle size. The model identifies reactions R7−R10 as necessary components to explain the accelerated, almost linear decay of OA and I toward the end of the reaction. It also shows that reaction R11—leading to formation of volatile products—is necessary to qualitatively reproduce the observed decrease of the droplet size. The necessity to account for reactions R7−R11 was confirmed through a sensitivity analysis performed by changing individually the value of each model parameter within 10%. Excluding reactions R7−R11, not even rough qualitative agreement could be reached with any reasonable choice of model parameters (this even holds for changes larger than 10%). Of course, this model is too simple to describe all details of the complicated photochemistry. Therefore, we refrain from any kind of least-squares refinement of the model parameters. The main uncertainty still lies in the model itself and not in the exact values of the parameters so that a parameter refinement would not provide more insight at this stage.

4. CONCLUSION

Our study reveals that the kinetics of the photodegradation of oleic acid droplets by visible light is not influenced by the electric charge state of the droplets. The kinetics was found to be the same for uncharged droplets and droplets with positive charges of up to 10^4 elementary charges per droplet. Furthermore, no spectral differences were observed in the time-dependent Raman spectra between neutral and electrically charged droplets. Both observations clearly hint that neither the kinetics nor the reaction mechanism of the photodegradation of oleic acid droplets by visible light are influenced by the presence of electric charges, at least for charge states of up to 10^4 elementary charges. So far, the influence of the charge state on reactions in aerosol particles has hardly been investigated. The reported example will contribute to a clarification of the influence of electric charges on reactions in aerosol particles.

We have refined the reaction mechanism we proposed in a previous study by fitting a kinetic multilayer model to experimental data. The multilayer model takes into account chemical reactions and mass transport in the droplet and between the droplet and the surrounding gas phase. Good fits were obtained with a model that assumes photoexcitation of oleic acid into an excited state which subsequently decays into intermediates. Photoexcitation of the intermediates and subsequent decay leads to the formation of nonvolatile and volatile products. The data indicate that the nonvolatile products are involved in further reaction steps with oleic acid molecules after photoexcitation, which produce new intermediates and nonvolatile and volatile products. This model is a powerful tool to analyze the experimental data retrieved from the Raman spectra, but further information on the chemical composition is required for a final confirmation and refinement of the mechanism.

■ ASSOCIATED CONTENT

Supporting Information

The Supporting Information is available free of charge at https://pubs.acs.org/doi/10.1021/acs.jpca.2c01370.

Description of the mobility classification, description of the Monte Carlo simulations, additional data for a neutral oleic acid droplet and an oleic acid droplet from an unaltered aerosol, description of the scaling factors determined from TotalTAOS, and the UV−vis spectrum of oleic acid (PDF)

■ AUTHOR INFORMATION

Corresponding Author

Ruth Signorell − *Department of Chemistry and Applied Biosciences, ETH Zürich, 8093 Zürich, Switzerland;* orcid.org/0000-0003-1111-9261; Email: ruth.signorell@phys.chem.ethz.ch

Authors

Evelyne A. Parmentier − *Department of Chemistry and Applied Biosciences, ETH Zürich, 8093 Zürich, Switzerland*

Pablo Corral Arroyo − *Department of Chemistry and Applied Biosciences, ETH Zürich, 8093 Zürich, Switzerland*

Richard Gruseck − *Department of Chemistry and Applied Biosciences, ETH Zürich, 8093 Zürich, Switzerland;* orcid.org/0000-0002-2033-3369

Loren Ban − *Department of Chemistry and Applied Biosciences, ETH Zürich, 8093 Zürich, Switzerland*

Grégory David − *Department of Chemistry and Applied Biosciences, ETH Zürich, 8093 Zürich, Switzerland;* orcid.org/0000-0002-2129-3266

Complete contact information is available at: https://pubs.acs.org/10.1021/acs.jpca.2c01370

Notes

The authors declare no competing financial interest.

Data Availability. Data needed to evaluate the conclusions of the paper are presented in the paper or the Supporting Information or are deposited in the ETH Research Collection doi: 10.3929/ethz-b-000554684. Additional data related to this paper may be requested from the authors.

■ ACKNOWLEDGMENTS

We are very grateful to Prof. Martin Fierz for lending us the aerosol charger and the electrostatic precipitator, and to Markus Steger, Daniel Zindel, and David Stapfer from the shops of the Laboratory of Physical Chemistry for technical help. This work was supported by the Swiss National Science Foundation (Project No. 200020_200306) and the ETH Zurich.

REFERENCES

(1) Mbareche, H.; Morawska, L.; Duchaine, C. On the interpretation of bioaerosol exposure measurements and impacts on health. *J. Air Waste Manage. Assoc.* **2019**, *69* (7), 789−804.

(2) Pöschl, U. Atmospheric Aerosols: Composition, Transformation, Climate and Health Effects. *Angew. Chem., Int. Ed.* **2005**, *44* (46), 7520−7540.

(3) Finlayson-Pitts, B. J. Reactions at surfaces in the atmosphere: integration of experiments and theory as necessary (but not necessarily sufficient) for predicting the physical chemistry of aerosols. *Phys. Chem. Chem. Phys.* **2009**, *11* (36), 7760−7779.

(4) Meier, R. R.; Anderson, G. P.; Cantrell, C. A.; Hall, L. A.; Lean, J.; Minschwaner, K.; Shetter, R. E.; Shettle, E. P.; Stamnes, K. Actinic radiation in the terrestrial atmosphere. *J. Atmos. Sol.-Terr. Phys.* **1997**, *59* (17), 2111−2157.

(5) Zhong, J.; Kumar, M.; Anglada, J. M.; Martins-Costa, M. T. C.; Ruiz-Lopez, M. F.; Zeng, X. C.; Francisco, J. S. Atmospheric Spectroscopy and Photochemistry at Environmental Water Interfaces. *Annu. Rev. Phys. Chem.* **2019**, *70* (1), 45−69.

(6) George, C.; Ammann, M.; D'Anna, B.; Donaldson, D. J.; Nizkorodov, S. A. Heterogeneous Photochemistry in the Atmosphere. *Chem. Rev.* **2015**, *115* (10), 4218−4258.

(7) Vaida, V. Sunlight initiated atmospheric photochemical reactions. *Int. J. Photoenergy* **2005**, *7*, 61.

(8) Laskin, A.; Laskin, J.; Nizkorodov, S. A. Chemistry of Atmospheric Brown Carbon. *Chem. Rev.* **2015**, *115* (10), 4335−4382.

(9) Corral Arroyo, P.; Bartels-Rausch, T.; Alpert, P. A.; Dumas, S.; Perrier, S.; George, C.; Ammann, M. Particle-Phase Photosensitized Radical Production and Aerosol Aging. *Environ. Sci. Technol.* **2018**, *52* (14), 7680−7688.

(10) Zahardis, J.; Petrucci, G. A. The oleic acid-ozone heterogeneous reaction system: products, kinetics, secondary chemistry, and atmospheric implications of a model system - a review. *Atmos. Chem. Phys.* **2007**, *7* (5), 1237−1274.

(11) Vesna, O.; Sax, M.; Kalberer, M.; Gaschen, A.; Ammann, M. Product study of oleic acid ozonolysis as function of humidity. *Atmos. Environ.* **2009**, *43* (24), 3662−3669.

(12) Gallimore, P. J.; Griffiths, P. T.; Pope, F. D.; Reid, J. P.; Kalberer, M. Comprehensive modeling study of ozonolysis of oleic acid aerosol based on real-time, online measurements of aerosol composition. *J. Geophys. Res.: Atmos.* **2017**, *122* (8), 4364−4377.

(13) Lee, A. K. Y.; Chan, C. K. Single particle Raman spectroscopy for investigating atmospheric heterogeneous reactions of organic aerosols. *Atmos. Environ.* **2007**, *41* (22), 4611−4621.

(14) Zhang, X.; Barraza, K. M.; Upton, K. T.; Beauchamp, J. L. Time resolved study of hydroxyl radical oxidation of oleic acid at the air-water interface. *Chem. Phys. Lett.* **2017**, *683*, 76−82.

(15) King, M. D.; Rennie, A. R.; Pfrang, C.; Hughes, A. V.; Thompson, K. C. Interaction of nitrogen dioxide (NO2) with a monolayer of oleic acid at the air−water interface − A simple proxy for atmospheric aerosol. *Atmos. Environ.* **2010**, *44* (14), 1822−1825.

(16) Docherty, K. S.; Ziemann, P. J. Reaction of Oleic Acid Particles with NO3 Radicals: Products, Mechanism, and Implications for Radical-Initiated Organic Aerosol Oxidation. *J. Phys. Chem. A* **2006**, *110* (10), 3567−3577.

(17) Parmentier, E. A.; David, G.; Arroyo, P. C.; Bibawi, S.; Esat, K.; Signorell, R. Photochemistry of single optically trapped oleic acid droplets. *J. Aerosol Sci.* **2021**, *151*, 105660.

(18) David, G.; Esat, K.; Ritsch, I.; Signorell, R. Ultraviolet broadband light scattering for optically-trapped submicron-sized aerosol particles. *Phys. Chem. Chem. Phys.* **2016**, *18* (7), 5477−5485.

(19) Whitby, K. T.; Liu, B. Y. H. Polystyrene aerosols—electrical charge and residue size distribution. *Atmospheric Environment (1967)* **1968**, *2* (2), 103−116.

(20) Flagan, R. C. Electrical Mobility Methods for Submicrometer Particle Characterization. *Aerosol Measurement* **2011**, 339−364.

(21) Forsyth, B.; Liu, B. Y. H.; Romay, F. J. Particle Charge Distribution Measurement for Commonly Generated Laboratory Aerosols. *Aerosol Sci. Technol.* **1998**, *28* (6), 489−501.

(22) Banerjee, S.; Gnanamani, E.; Yan, X.; Zare, R. N. Can all bulk-phase reactions be accelerated in microdroplets? *Analyst* **2017**, *142* (9), 1399−1402.

(23) Wilson, K. R.; Prophet, A. M.; Rovelli, G.; Willis, M. D.; Rapf, R. J.; Jacobs, M. I. A kinetic description of how interfaces accelerate reactions in micro-compartments. *Chemical Science* **2020**, *11* (32), 8533−8545.

(24) Crawford, E. A.; Esen, C.; Volmer, D. A. Real Time Monitoring of Containerless Microreactions in Acoustically Levitated Droplets via Ambient Ionization Mass Spectrometry. *Anal. Chem.* **2016**, *88* (17), 8396−8403.

(25) Bain, R. M.; Pulliam, C. J.; Thery, F.; Cooks, R. G. Accelerated Chemical Reactions and Organic Synthesis in Leidenfrost Droplets. *Angew. Chem., Int. Ed.* **2016**, *55* (35), 10478−10482.

(26) Li, Y.; Liu, Y.; Gao, H.; Helmy, R.; Wuelfing, W. P.; Welch, C. J.; Cooks, R. G. Accelerated Forced Degradation of Pharmaceuticals in Levitated Microdroplet Reactors. *Chem. - Eur. J.* **2018**, *24* (29), 7349−7353.

(27) Lee, J. K.; Samanta, D.; Nam, H. G.; Zare, R. N. Micrometer-Sized Water Droplets Induce Spontaneous Reduction. *J. Am. Chem. Soc.* **2019**, *141* (27), 10585−10589.

(28) Wei, Z.; Li, Y.; Cooks, R. G.; Yan, X. Accelerated Reaction Kinetics in Microdroplets: Overview and Recent Developments. *Annu. Rev. Phys. Chem.* **2020**, *71* (1), 31−51.

(29) Xiong, H.; Lee, J. K.; Zare, R. N.; Min, W. Strong Electric Field Observed at the Interface of Aqueous Microdroplets. *J. Phys. Chem. Lett.* **2020**, *11* (17), 7423−7428.

(30) Cremer, J. W.; Thaler, K. M.; Haisch, C.; Signorell, R. Photoacoustics of single laser-trapped nanodroplets for the direct observation of nanofocusing in aerosol photokinetics. *Nat. Commun.* **2016**, *7* (1), 10941.

(31) Corral Arroyo, P.; David, G.; Alpert, P. A.; Parmentier, E. A.; Ammann, M.; Signorell, R. Amplification of light within aerosol particles accelerates in-particle photochemistry. *Science* **2022**, *376* (6590), 293−296.

(32) Ahmed, M.; Blum, M.; Crumlin, E. J.; Geissler, P. L.; Head-Gordon, T.; Limmer, D. T.; Mandadapu, K. K.; Saykally, R. J.; Wilson, K. R. Molecular Properties and Chemical Transformations Near Interfaces. *J. Phys. Chem. B* **2021**, *125* (32), 9037−9051.

(33) Nissenson, P.; Knox, C. J. H.; Finlayson-Pitts, B. J.; Phillips, L. F.; Dabdub, D. Enhanced photolysis in aerosols: evidence for important surface effects. *Phys. Chem. Chem. Phys.* **2006**, *8* (40), 4700−4710.

(34) Shaik, S.; Ramanan, R.; Danovich, D.; Mandal, D. Structure and reactivity/selectivity control by oriented-external electric fields. *Chem. Soc. Rev.* **2018**, *47* (14), 5125−5145.

(35) Huang, X.; Tang, C.; Li, J.; Chen, L.-C.; Zheng, J.; Zhang, P.; Le, J.; Li, R.; Li, X.; Liu, J.; et al. Electric field-induced selective catalysis of single-molecule reaction. *Sci. Adv.* **2019**, *5* (6), eaaw3072.

(36) Jacobs, M. I.; Davies, J. F.; Lee, L.; Davis, R. D.; Houle, F.; Wilson, K. R. Exploring Chemistry in Microcompartments Using Guided Droplet Collisions in a Branched Quadrupole Trap Coupled to a Single Droplet, Paper Spray Mass Spectrometer. *Anal. Chem.* **2017**, *89* (22), 12511−12519.

(37) Rovelli, G.; Jacobs, M. I.; Willis, M. D.; Rapf, R. J.; Prophet, A. M.; Wilson, K. R. A critical analysis of electrospray techniques for the determination of accelerated rates and mechanisms of chemical reactions in droplets. *Chem. Sci.* **2020**, *11* (48), 13026−13043.

(38) Liu, B. Y. H.; Lee, K. W. An aerosol generator of high stability. *Am. Ind. Hyg. Assoc. J.* **1975**, *36* (12), 861−865.

(39) Dhaniyala, S.; Fierz, M.; Keskinen, J.; Marjamäki, M. Instruments Based on Electrical Detection of Aerosols. *Aerosol Meas.* **2011**, 393−416.

(40) Fierz, M.; Houle, C.; Steigmeier, P.; Burtscher, H. Design, Calibration, and Field Performance of a Miniature Diffusion Size Classifier. *Aerosol Sci. Technol.* **2011**, *45* (1), 1−10.

(41) Weingartner, E.; Burtscher, H.; Hüglin, C.; Ehara, K. Semi-Continuous Mass Measurement. *Aerosol Meas.* **2011**, 255−268.

https://doi.org/10.1021/acs.jpca.2c01370
J. Phys. Chem. A 2022, 126, 4456−4464

(42) Ban, L.; Gartmann, T. E.; Yoder, B. L.; Signorell, R. Low-Energy Electron Escape from Liquid Interfaces: Charge and Quantum Effects. *Phys. Rev. Lett.* **2020**, *124* (1), 013402.
(43) Chadha, T. S.; Chattopadhyay, S.; Venkataraman, C.; Biswas, P. Study of the Charge Distribution on Liposome Particles Aerosolized by Air-Jet Atomization. *J. Aerosol Med. Pulm. Drug Delivery* **2012**, *25* (6), 355−364.
(44) Matsoukas, T. The Coagulation Rate of Charged Aerosols in Ionized Gases. *J. Colloid Interface Sci.* **1997**, *187* (2), 474−483.
(45) David, G.; Esat, K.; Hartweg, S.; Cremer, J.; Chasovskikh, E.; Signorell, R. Stability of aerosol droplets in Bessel beam optical traps under constant and pulsed external forces. *J. Chem. Phys.* **2015**, *142* (15), 154506.
(46) Shiraiwa, M.; Pfrang, C.; Pöschl, U. Kinetic multi-layer model of aerosol surface and bulk chemistry (KM-SUB): the influence of interfacial transport and bulk diffusion on the oxidation of oleic acid by ozone. *Atmos. Chem. Phys.* **2010**, *10* (8), 3673−3691.
(47) Rademann, K. P. W. Atkins: Physical Chemistry, 4th Edition, Oxford University Press, Oxford, ISBN 0-19-855284-X, 1990. 995 Seiten, Preis: £ 19.50 (Paperback). *Berichte der Bunsengesellschaft für physikalische Chemie* **1990**, *94* (10), 1171−1171.
(48) Aiona, P. K.; Lee, H. J.; Lin, P.; Heller, F.; Laskin, A.; Laskin, J.; Nizkorodov, S. A. A Role for 2-Methyl Pyrrole in the Browning of 4-Oxopentanal and Limonene Secondary Organic Aerosol. *Environ. Sci. Technol.* **2017**, *51* (19), 11048−11056.
(49) Laskin, J.; Laskin, A.; Roach, P. J.; Slysz, G. W.; Anderson, G. A.; Nizkorodov, S. A.; Bones, D. L.; Nguyen, L. Q. High-Resolution Desorption Electrospray Ionization Mass Spectrometry for Chemical Characterization of Organic Aerosols. *Anal. Chem.* **2010**, *82* (5), 2048−2058.
(50) Walser, M. L.; Park, J.; Gomez, A. L.; Russell, A. R.; Nizkorodov, S. A. Photochemical Aging of Secondary Organic Aerosol Particles Generated from the Oxidation of d-Limonene. *J. Phys. Chem. A* **2007**, *111* (10), 1907−1913.
(51) Canonica, S.; Hellrung, B.; Wirz, J. Oxidation of Phenols by Triplet Aromatic Ketones in Aqueous Solution. *J. Phys. Chem. A* **2000**, *104* (6), 1226−1232.
(52) McNeill, K.; Canonica, S. Triplet state dissolved organic matter in aquatic photochemistry: reaction mechanisms, substrate scope, and photophysical properties. *Environ. Sci.: Processes Impacts* **2016**, *18* (11), 1381−1399.

https://doi.org/10.1021/acs.jpca.2c01370
J. Phys. Chem. A 2022, 126, 4456−4464